



Support-free laser-based powder bed fusion of metals using pulsed exposure strategies

Jonas Grünewald¹ · Jonas Reinelt¹ · Holger Sedlak² · Katrin Wudy¹

Received: 10 August 2022 / Accepted: 4 March 2023 / Published online: 31 March 2023
© The Author(s) 2023

Abstract

Several studies demonstrate the potential of pulsed exposure strategies for improving spatial accuracy, surface quality, and manufacturability of low-angle overhangs in laser-based powder bed fusion of metals. In this paper, those fundamental potentials are transferred to the support-free manufacturing of heat exchanger structures with partial horizontal overhangs made of Ti6Al4V. The pulsed exposure with pulse repetition rates of 20 kHz and pulse duration of 25 μ s enabled the support-free manufacturing of these complex structures with densities of more than 99%. A comparison of the Archimedean density determination with optical density determination using micrographs indicate permeability of the specimens below an applied volume energy density of 30 J/mm³ due to open porosity. Furthermore, the pulsed manufactured structures show an improved flow behavior within the heat exchanger compared to specimens manufactured with continuous exposure strategies.

Keywords Additive manufacturing · Titanium alloy · Ti6Al4V · Heat exchanger · Power modulation

1 Introduction and state of the art

In laser-based powder bed fusion of metals (PBF-LB/M), metallic components are manufactured by selectively melting and fusing individual powder layers by means of a laser. The layer-by-layer manufacturing process creates geometrical freedom that is beyond the scope of conventional machining processes. Therefore, PBF-LB/M is steadily establishing as an industrial manufacturing process.

State-of-the-art is the vector-based exposure of the powder bed using continuous wave (cw) emission of the laser. This strategy results in high-energy inputs on a small spatial scale, which may implicate overheating or heat accumulation, especially for structures with flat overhang angles [1, 2]. As a result, thermal distortion frequently occurs in overhang areas [3]. Consequently, the manufacturing of overhang structures using PBF-LB/M is challenging. To prevent

distortions and accumulated heat, external support structures are typically used during PBF-LB/M. This reinforces the overhang structure and allows heat to be dissipated from the process zone. Designing and manufacturing support structures is a distinct field of research that includes investigating how to quickly dissipate heat [3, 4] and how to easily remove the supports [4, 5]. In powder bed fusion of metals using an electron beam, even contact-free support structures have been demonstrated [6]. However, it is not possible to remove the support structures of complex components in many cases.

To reduce the amount of post-processing required and to enable the manufacturing of complex components, the aim of this paper is to achieve a PBF-LB/M process without support structures. To overcome the challenge of support-free PBF-LB/M, one approach is to tailor the energy input to adjust the thermal budget during processing. This tailoring can be implemented using pulsed exposure strategies.

Pulsed emission of a laser means that energy is emitted only during the duration of the laser pulse τ_{pulse} . If the peak power of the pulse is equal to the cw power, the average power emitted is reduced to the duty cycle fraction δ . The duty cycle describes the time share of the pulse duration in the period duration of the pulsed emission and is defined as

$$\delta = v_{rep} \cdot \tau_{pulse} \quad (1)$$

✉ Jonas Grünewald
jonas.gruenewald@tum.de

¹ Professorship of Laser-based Additive Manufacturing, Department of Mechanical Engineering, TUM School of Engineering and Design, Technical University of Munich, Boltzmannstr. 15, 85748 Garching, Germany

² Justairtech GmbH, Hohenlindener Str. 1, 81677 Munich, Germany

with the pulse repetition rate v_{rep} .

The advantages of pulsed PBF-LB/M have been discussed for processing various metal alloys containing the objectives to

- improve the component surface quality [7–10],
- tailor the microstructure [11–14],
- increase spatial accuracy [10, 14–20], and
- manufacture support-free overhang structures [9, 10].

Pulsed exposure with low repetition rates within the magnitude of Hz, increased overlap, and reduced scanning speed results in lower top and side surface roughness [7, 8]. The application of pulsed exposure with high repetition rates of 20 kHz has the potential to reduce the downskin surface roughness [9]. Moreover, due to the frequently used pulse overlap and discrete solidification of individual melt pools, the surface roughness has less direction-dependent texture [10].

Karami et al. [14] proved that a microstructure with increased homogeneity is produced with pulsed exposure of Ti6Al4V lattice structures. This results in isotropic component properties and increased yield stress [14]. Furthermore, the microstructure of aluminum and nickel-based alloys can be tailored using pulsed exposure, as shown in [11] for AlSi12 and AlSi10Mg, in [13] for AlSi10Mg, and in [12] for IN738LC.

Caprio et al. [15, 16], Demir et al. [17–19], Karami et al. [14], Laag et al. [10] and Laitinen et al. [20] successfully demonstrated increased geometrical accuracy of parts using pulsed PBF-LB/M due to smaller melt pools. The smaller melt pools are caused from a lower melting efficiency in pulsed processing [16]. Consequently, the deposition volume [15] and the build rate [16] tend to be reduced using pulsed PBF-LB/M. Laag et al. [10] found smaller melt pools result in less entrainment of powder particles, which additionally maintains a small melt pool volume. Laitinen et al. [20] report a larger pulse overlap is required for the generation of continuous melt tracks at shorter pulse durations. Consequently, components manufactured with constant fluence tend to have higher densities when manufactured with longer pulse durations or rather larger duty cycles [18]. In addition to the temporal energy input, the component densities depend on the geometry. When constant parameters are used, heat accumulation can occur in narrow component areas, while undermelting occurs in solid component areas [19]. Therefore, process parameters should be adjusted depending on the feature size. Pulsed exposure has a positive impact especially in fine geometries [14, 18]. To utilize the potentials for filigree structures while maintaining high productivity, combinations of pulsed and cw exposures are recommended [10, 19]. Accordingly, filigree areas as well as overhangs are processed with pulsed exposure and solid

areas are exposed with cw. The combination results in similar melt pool sizes during processing for both areas [10, 19]. Based on these findings, a layer-by-layer control of the process parameters was developed at the Politecnico di Milano [21, 22]. The control system uses a coaxial camera to detect the size of the melt pool and adjusts the duty cycle in critical areas during the subsequent layer [21, 22]. This results in increased process stability with constant melt pool sizes and less defects starting from the second layer [21, 22].

Regarding support-free PBF-LB/M, preliminary investigations [9] demonstrate the manufacturability of flat-angle overhang structures without support structures. In these experiments, the overhang angle was reduced from 25° to down to 15° using pulsed PBF-LB/M. Demir et al. [17] proved the potential of pulsed PBF-LB/M for support-free manufacturing of filigree structures on stents as lattice structures. However, to avoid support structures, a design with self-supporting bridges with overhang angles of 45° was used [17].

The realization of complex structures (such as internal cooling channels and heat exchanger structures) requires support-free manufacturing of flat overhangs as well as increased surface quality and spatial accuracy. Therefore, this study transfers the presented fundamental potentials of pulsed exposure strategies to the manufacturing of specific patent-pending heat exchanger structures with partial horizontal overhang structures. The research objective is the investigation of the influence of the pulsed PBF-LB/M process on resulting component properties of the heat exchanger structures (density, wall thickness and pressure drop during flow). The aim is to achieve constant wall thicknesses at high densities and low pressure drops.

2 Approach and methodology

A parameter study on an industrial demonstrator specimen is conducted to demonstrate the potential of pulsed exposure strategies on support-free PBF-LB/M. The experimental setup and the investigated materials, specimens, parameter sets, and component properties are presented in the following.

2.1 Experimental setup

Test specimens were manufactured using a modified PBF-LB/M system EOS M280 (EOS GmbH, Krailling, Germany). The system is designed to use cw exposure only. It is equipped with a 400 W fiber laser (IPG Laser GmbH, Burbach, Germany) with a resulting spot size of approximately 100 μm [23]. Modern fiber lasers enable fast power modulation and can, thus, realize a pulsed energy output [24]. Pulses with durations in the range of microseconds

and repetition rates up to multiple kHz are possible [24]. To achieve pulsing with the experimental system, the gate signal is periodically interrupted. An optocoupler circuit is integrated for this purpose. The pulse frequency is set by a galvanically decoupled function generator. Due to the response time of the optocoupler, the setup is limited to a maximum repetition rate of 25 kHz.

The response of the laser beam source to the pulsed gate signal is verified via weld-in tests. For this purpose, pulsed single weld tracks are created in a sheet at high scanning speeds v_{scan} of 4000 mm/s, 5000 mm/s, 6000 mm/s, and 7000 mm/s as well as different duty cycles δ of 0.4, 0.5, and 0.6. The high scanning speeds prevent overlapping of the laser pulses. For measuring the manufactured weld tracks, a 3D profilometer (Keyence VR-3100, Ōsaka, Japan) is used. From the measured data, the existing duty cycles are determined by comparing the length of the gap between the weld of two laser pulses l_{gap} with the theoretical distance traveled during the laser pulse pause. The shape of the individual pulse tracks is assumed to be an oblong hole with the width w_{pulse} (see Fig. 1(a)). The measured duty cycle $\delta_{measured}$ is calculated by

$$\delta_{measured} = 1 - \frac{v_{rep}(l_{gap} + w_{pulse})}{v_{scan}} \quad (2)$$

To ensure the worst case with regard to the pulse rise time is represented, a peak power of 370 W is used during the experiments. Figure 2 shows the measured duty cycles, which match very well with the set duty cycles. The duty cycle increase at low scanning speeds is assumed to be due to heat accumulation during the exposure. Consequently, the pulse tracks become wider in the center and thus, the

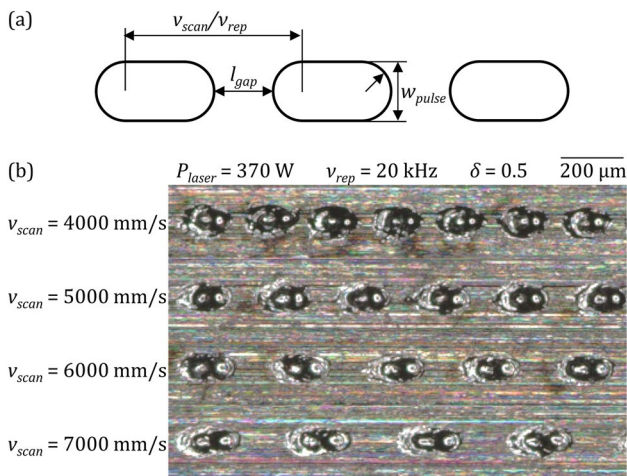


Fig. 1 a Schematic illustration of the weld-in experiments and b top views of the weld tracks

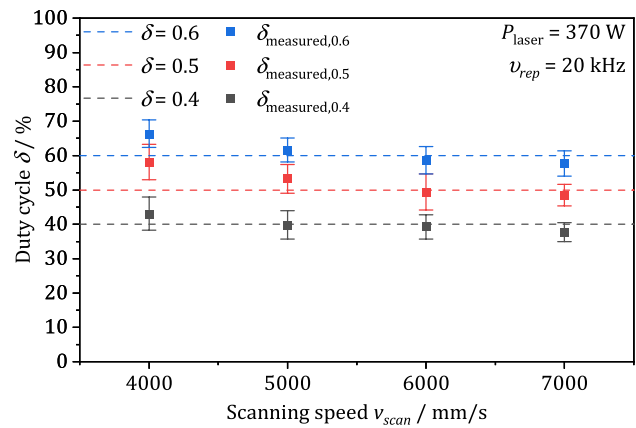


Fig. 2 Measured duty cycles $\delta_{measured}$ compared to set duty cycles δ , determined at four different scanning speeds v_{scan} with constant laser power P_{laser} and pulse repetition rate v_{rep}

assumption of the oblong hole shape is no longer valid (see Fig. 1(b)).

2.2 Feedstock material

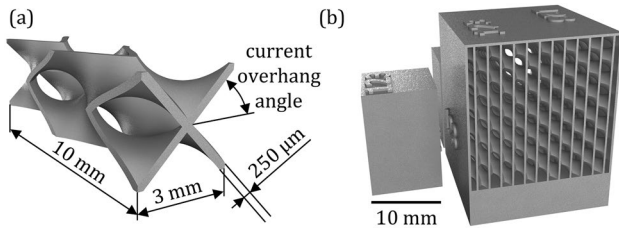
In this study, Ti6Al4V substrates and powders are used. Offering a density of 4.43 g/cm³, the Ti6Al4V exhibits good strength, ductility, and fracture toughness, as well as corrosion and temperature resistance. The powder is provided by TLS Technik GmbH & Co. Spezialpulver KG (Bitterfeld, Germany). The particle size distribution is determined using laser diffraction according to ISO 13320. The characteristic particle diameters are identified as $D_{10,3} = 34.5 \mu\text{m}$, $D_{50,3} = 45.7 \mu\text{m}$, and $D_{90,3} = 58.1 \mu\text{m}$. Table 1 shows the chemical composition of the powder.

2.3 Test specimens and build job design

Heat exchangers are an excellent use case for PBF-LB/M. With the geometric freedom and high level of manufacturing precision of PBF-LB/M, structures can be manufactured specifically for optimized heat transfer and fluid flow. In this publication, a specific patents-pending structure of an air-to-air heat exchanger (justairtech GmbH, Munich, Germany) is used as a specimen. The elementary cell of this structure is shown in Fig. 3(a). It consists of four quadratically cut helices, where each helix is symmetrical to the neighboring one. The heat exchange is based on the heat transfer between directly adjacent channels. Therefore, the heat conduction of the structure is only of minor importance. More important is a high heat transfer at the channel walls with a low pressure drop inside the structure. By setting the size of the helix cutout, the size of each channel is adjusted. The curvature of the channels is determined by the pitch of the helices. This design allows the direction of the structure to be tailored. The structure can be

Table 1 Chemical composition

N (%)	C (%)	H (%)	Fe (%)	O (%)	Al (%)	V (%)	Ti (%)
0.005	0.006	0.001	0.19	0.09	6.34	4.08	Bal

**Fig. 3** CAD models of (a) an elementary cell of the air-to-air heat exchanger and (b) the test specimens cuboid and heat exchanger structure

directed around corners or curves. As a result, elementary cells may appear in various orientations in a single component. Due to the geometric freedom and complexity of the structures, overhangs can appear at all angles and support structures cannot be removed.

As test specimens, heat exchanger structures are created from 6×6 elementary cells with a cutout size of 3 mm and a pitch of 10 mm. The specimens include channels with two complete rotations and are sealed by $300 \mu\text{m}$ walls on the sides, bottom, and top, resulting in outer dimensions of $18.6 \times 18.6 \times 20 \text{ mm}^3$. The wall thickness b_w of the structures is set to $250 \mu\text{m}$. To perform a worst-case analysis during the manufacturing of the structures, the helix axes of the structures are oriented parallel to the building platform. This creates partial horizontal overhangs. An orientation of the helix axes in the building direction results in pitch-dependent constant (simpler to manufacture) angles of the walls.

In addition, solid cuboids ($10 \times 10 \times 10 \text{ mm}^3$) are built for density determination. All parts contain a massive 5 mm support to later be cut off from the build platform, see Fig. 3(b). The specimens are arranged at an azimuth angle of 45° to the coating and gas flow direction as recommended in VDI 3405 Part 2.

2.4 Process parameter

The process parameters laser power P_{laser} , scanning speed v_{scan} , and hatch distance h are varied within a full factorial design of the experiments. These process parameters can be combined with the constant powder layer thickness t_{powder} , pulse repetition rate v_{rep} , and pulse duration τ_{pulse} to form the volume energy density

$$E_v = \frac{P_{laser} \cdot v_{rep} \cdot \tau_{pulse}}{v_{scan} \cdot h \cdot t_{powder}} \quad (3)$$

Table 2 The three levels of varied process parameters

Level	1	2	3
Hatch distance h	100 μm	80 μm	60 μm
Scanning speed v_{scan}	1,250 mm/s	1,000 mm/s	750 mm/s
Laser power P_{laser}	180 W	210 W	245 W

Based on preliminary experiments [9] the levels of laser power P_{laser} , scanning speed v_{scan} and hatch distance h are chosen as listed in Table 2. The constant process parameters are set to $t_{powder} = 40 \mu\text{m}$, $v_{rep} = 20 \text{ kHz}$ and $\tau_{pulse} = 25 \mu\text{s}$. The pulse duration and repetition rate are also adopted from preliminary investigations [9]. The layer thickness is slightly reduced in this study in order to achieve a higher resolution in the build direction. For each parameter set, two heat exchanger structures and four cuboids are manufactured. In summary, a total of 27 parameter sets, 52 heat exchanger structures, and 104 cuboids are investigated. All areas of each specimen (Contour, Upskin, Downskin) were manufactured with the same parameter set. Furthermore, the specimens are manufactured without beam offset. This enables a quantitative investigation of the deviations from the nominal contour.

2.5 Analysis of component properties

Dimensional accuracy, density and pressure drop during air flow are investigated on the test specimens. For determination of the dimensional accuracy, the heat exchanger structures are separated using wire eroding. The cutting thickness of the eroding wire creates two planes that are analyzed (see Fig. 4). The wall thicknesses b_w are measured in these planes (at current overhang angles of 45° and 30°) using a 3D profilometer (Keyence VR-3100, Ōsaka, Japan).

The density of the cuboids is determined using the Archimedeian method according to DIN EN ISO 3369. To determine the relative density ρ_{rel} , the solid density of Ti6Al4V is assumed to be 4.43 g/cm^3 . In addition, the density of the cuboids is determined optically based on micrographs. For this purpose, the specimens are embedded in a transparent epoxy, ground in five stages using silicon carbide paper (grit 180, 320, 800, 1,200 and 2,500), and polished in two stages using cloths and diamond pastes ($3 \mu\text{m}$ and $1 \mu\text{m}$). Prior to the polishing steps, the specimens are ultrasonically washed to remove loose and adhering powder particles. The micrograph images are taken at four locations per cuboid at a $2.5 \times$ magnification using a reflected light microscope

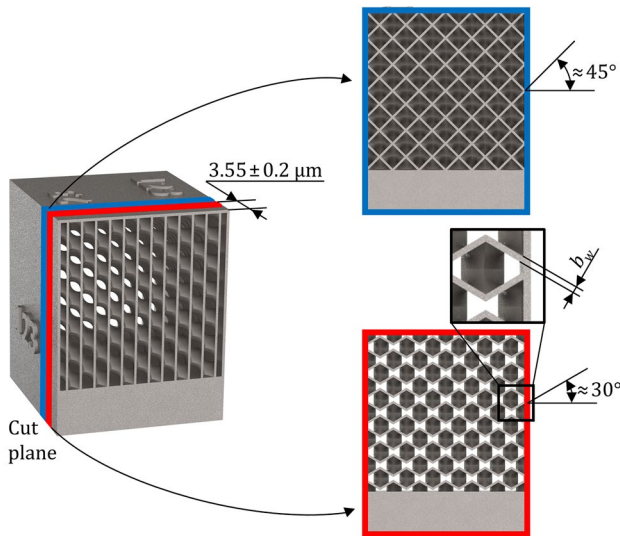


Fig. 4 Schematic of the cut plane of the heat exchanger structure and the measurement planes for the wall thickness b_w

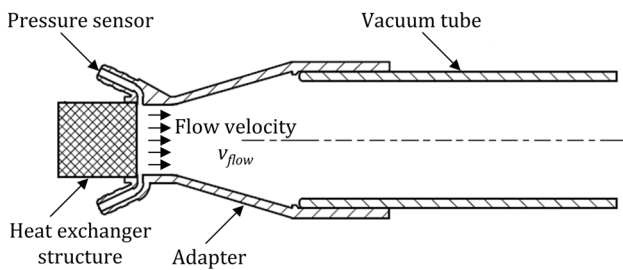


Fig. 5 Drawing of the measurement setup for determining the pressure drop p_{drop} as a function of the flow velocity v_{flow}

(Nikon MM-40, Tokyo, Japan). The size of the images (1200×1600 pixels) with a proportion factor of $1.957 \mu\text{m}/\text{pixel}$ result in an area of about 7.35 mm^2 per image. This implies an investigated cross-sectional area of about 30 mm^2 per cuboid. Finally, the images are binarized and evaluated.

To characterize the air flow behavior within the heat exchanger structures, the pressure drop is determined as a function of the flow velocity. For this purpose, the heat exchanger structures are individually mounted in an adapter that connects the heat exchanger channels to a vacuum tube (see Fig. 5). In the adapter, two BME280 pressure sensors (Bosch Sensortec GmbH, Reutlingen, Germany) are installed next to the heat exchanger. For one measurement, five flow velocities are applied that are measured using a Venturi tube. Each heat exchanger structure is measured twice. Within the second measurement, the structure is inverted so that the fluid flows through the structure in the reverse direction. The measured pressure drops p_{drop} are mapped to calculated flow velocities v_{flow} through the heat exchanger (see Fig. 6). The

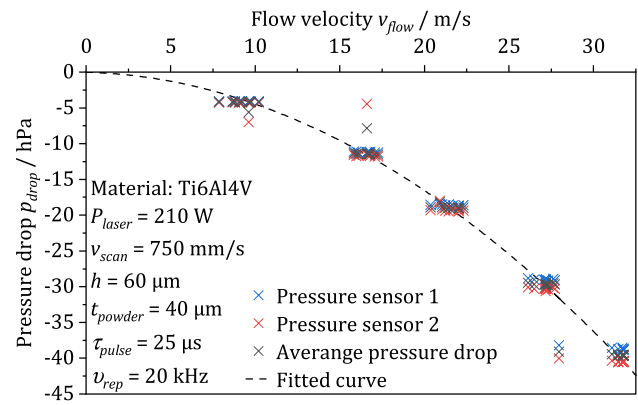


Fig. 6 Exemplary evaluation of a pressure drop measurement inside a heat exchanger structure manufactured with the listed process parameters

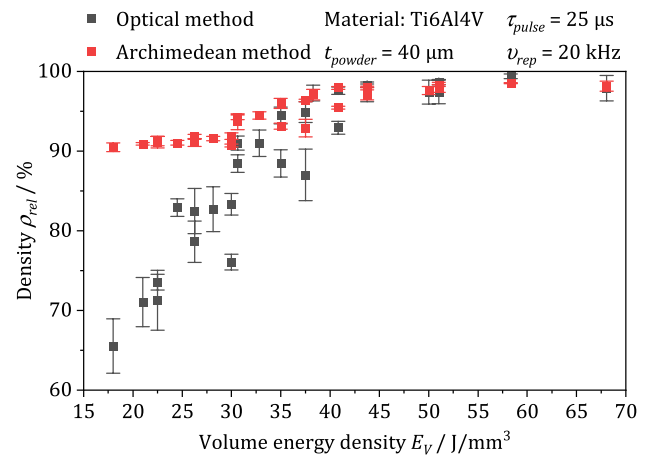


Fig. 7 Relative densities of cuboids ρ_{rel} determined by optical and Archimedean methods as a function of volume energy density E_v

mean values are used to calculate a 2nd degree polynomial trend line function forced through the origin (dotted line in Fig. 6). The resulting functions are a characteristic of the pressure drop depending on the process parameters used.

3 Results and discussion

The results are presented in the order of the influence of pulsed exposure on the specimen density, the dimensional accuracy, and on resulting flow properties within the heat exchanger structures.

3.1 Influence of pulsed exposure on density

Figure 7 shows the densities of the cubic specimens as a function of the volume energy densities E_v according to Eq. 3. The densities were determined using the optical and

the Archimedean method to find the critical density value for infiltrated structures. The measured values from the optical density determination increase almost linearly up to a volume energy density of 35 J/mm^3 . Above 35 J/mm^3 , the density values approximate 100% asymptotically, with the maximum density (above 99%) achieved at about 58 J/mm^3 . The density values determined using the Archimedean method follow a rather s-shaped trend. Until approximately 30 J/mm^3 , the density values increase in an almost linear manner. Between 30 and 40 J/mm^3 , the increase is steeper. From approximately 40 J/mm^3 , the density values settle in a range above 97.5%. The results of the optical and Archimedean method are almost equal above a transition range between 30 and 35 J/mm^3 . For energy densities less than 30 J/mm^3 , the measured densities differ significantly between the two measurement methods.

The discrepancy between the methods for low energy densities can be explained by the infiltration of the specimens with the liquid during Archimedean density determination. The Archimedean method according to DIN EN ISO 3369 is only valid for impermeable materials. If the measuring liquid infiltrates the specimen, the pores are not included in the specimen volume. Consequently, the resulting density values seem to be higher. The reason for the infiltration is the presence of open porosity in the corresponding specimens manufactured with low volume energy densities E_v . This open porosity can be seen in the micrograph in Fig. 8(a). In the volume energy density range between 30 and 35 J/mm^3 , closed voids are formed instead of open porosity (see Fig. 8(b)). Therefore, the density analysis methods provide comparable values in and above this range. With further increasing volume energy density, the volume of these voids decreases (see Fig. 8(c)), resulting in increased relative densities.

The use of both the optical and Archimedean density determination method is beneficial to the later analyses of the flow behavior and pressure drop. The threshold at which

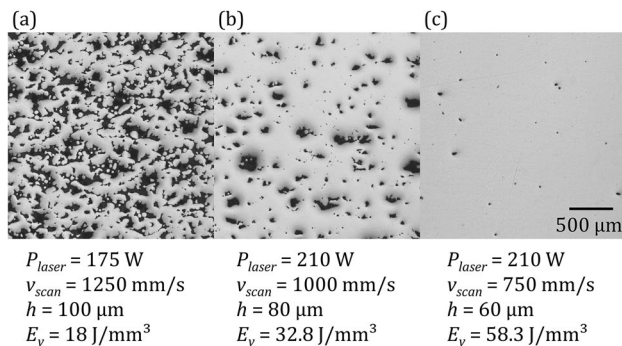


Fig. 8 Micrographs of three selected cuboids manufactured with a volume energy density of (a) 18 J/mm^3 , (b) 32.8 J/mm^3 , and (c) 58.3 J/mm^3 .

the density values of the two measurement methods diverge represents the threshold of infiltration of the specimens with fluids. Heat exchanger structures should only transfer the heat of the fluids in the channels. An exchange of fluid between the channels must be avoided. Beneath the threshold of volume energy density divergence (approximately 30 J/mm^3 in this study), it is likely that the walls are traversed by the fluid and a mass transfer occurs.

Figure 9 contains photos of the wire-eroded cut surfaces of the heat exchanger specimens with the process parameters from Fig. 8. The images indicate similar densities of the heat exchanger structures as the densities of the cuboids. Figure 9(a) shows high porosity due to the irregular reflections of the cut surfaces. As the volume energy density increases, the reflections become more homogeneous (see Fig. 9(b)) until they are most homogeneous at the highest energy density (see Fig. 9(c)), indicating a qualitatively similar trend with respect to the relative density.

3.2 Influence of pulsed exposure on dimensional accuracy

The photos of the cut surfaces of the heat exchangers (see Fig. 9) show no obvious dependencies of the wall thicknesses on the process parameters used. The measured wall thicknesses b_w at current overhang angles of 30° and 45° are shown in Fig. 10. The measured values are almost constant for the chosen parameter sets and vary around a level of $330 \mu\text{m}$. It was expected that different levels of the varied process parameters as well as the corresponding volume energy densities would have a bigger effects on the wall

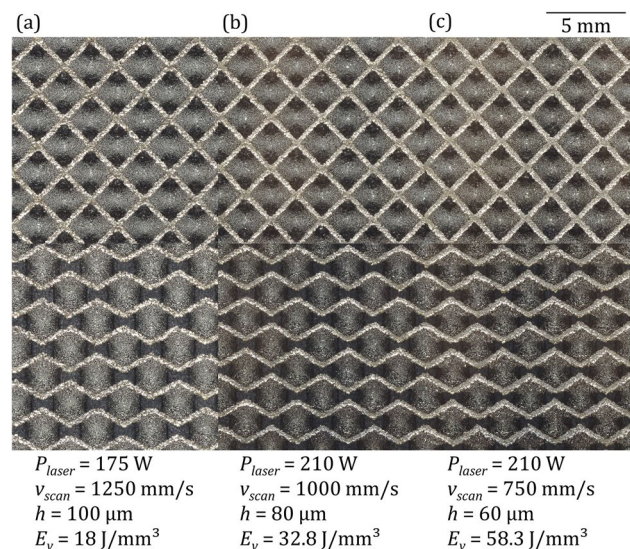


Fig. 9 Photos of the cut surfaces of three selected specimens with a volumetric energy density of (a) 18 J/mm^3 , (b) 32.8 J/mm^3 , and (c) 58.3 J/mm^3 .

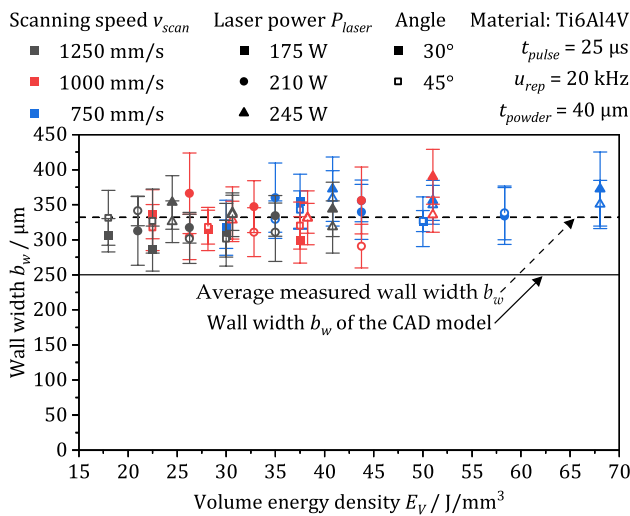


Fig. 10 Wall widths b_w at various angles as a function of volume energy density E_v

thickness, since the resulting melt pool should become wider and penetrate deeper into the powder bed [25]. The expected influences cannot be observed in Fig. 10.

Moreover, multiple regression analyses (see Table 3) do not show a clear influence of the varied process parameters on the wall thicknesses. The analyses show a high significance for the laser power and the scanning speed. However, the calculated coefficients are in a very small range close to zero. Therefore, the impact of changes in these parameters on the change in wall thickness is very low. Considering the standardized coefficients, the laser power has the largest influence of all process parameters on the wall thickness of the 30° walls. For the wall thickness of the 45° walls, the scanning speed has a slightly bigger influence. Although all the measured values of the wall widths are almost constant, the regression analyses clearly identified independence of the hatch spacing with the wall widths, which is indicated by the low significance (p -value). In addition to the small values

of the coefficients, the low coefficients of determination R^2 of 15.4% and 7% indicate low influence of the individual process parameters on the resulting wall thickness.

Nevertheless, for both angular positions, the averaged measured wall thicknesses are approximately 80 μm larger than the wall thicknesses of the CAD model (solid line at 250 μm). This indicates melt track widths of approximately 80 μm since no beam offset was used in the build job. This value is relatively small compared to the specified spot size of 100 μm [23]. The measured wall thicknesses confirm the finding that pulsed exposure allows an increase in resolution due to smaller melt pool widths [18, 20]. Laitinen et al. [20] achieve melt track widths of 80 μm (similar to the spot size) for pulse lengths of 50 μs and pulse repetition rates in the range of 1 kHz in single track experiments with 316L. For increased pulse lengths up to cw, the melt track widths become larger [20]. Demir et al. [18] achieve melt track widths larger than the spot diameter for pulse durations larger than 70 μs and pulse repetition rates in the range of 12 kHz. Based on the current literature, it seems conclusive that pulse lengths of 25 μs and pulse repetition rates of 20 kHz result in melt track widths in a range smaller than the spot size. Furthermore, the comparatively short pulse duration may result in constant small melt pools due to the short interaction time.

The constant wall thicknesses imply that the generated channels of the heat exchanger have constant cross sections. The constant flow-through cross sections allow flow analyses on the influence of the process parameters used independent to the macroscopic geometry variations.

3.3 Impact on the flow behavior within the heat exchanger

Figure 11 summarizes the trend line functions of all investigated specimens. The different volume energy densities E_v are represented by a color code. In addition, the diagram shows two fitted data plots for heat exchanger structures

Table 3 Results of multiple regression analyses

Variable	Wall width $b_{w, 30^\circ}$		Wall width $b_{w, 45^\circ}$	
	Coefficient	Standardized coefficient	Coefficient	Standardized coefficient
Constant	267***		300.0***	
Laser power P_{laser}	0.582*** (0.109)	0.336***	0.247**	0.183**
Scanning speed v_{scan}	-0.0520*** (0.0141)	-0.230***	-0.0376**	-0.213**
Hatch h	-0.00521 (0.177)	-0.00185	0.143	0.0649
R^2 (corr)	0.154		0.0703	
$F(df=3; 212)$	14.0***		6.42***	

* $p < 0.05$, ** $p < 0.01$, *** $p < 0.001$

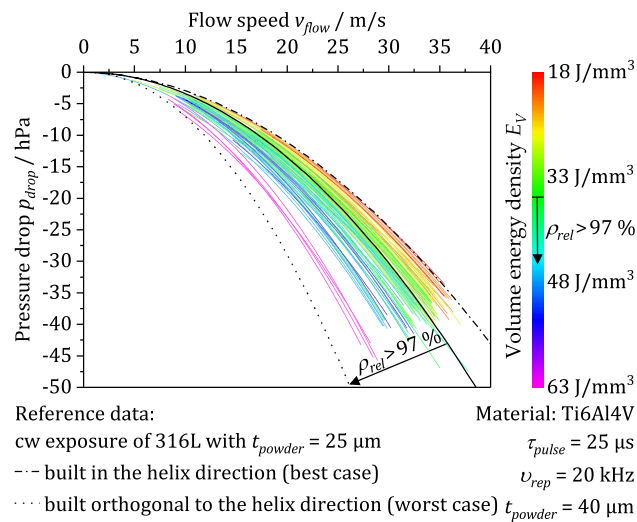


Fig. 11 Pressure drop p_{drop} as a function of the flow velocity v_{flow} depending on the exposure strategy and process parameters

with the same geometric dimensions made of 316L with cw exposure (black dash-dotted and dotted lines). The dash-dotted line represents the data of a heat exchanger structure built in the direction of the helix axis and the dotted line orthogonally to the helical direction. All specimens manufactured using pulsed PBF-LB/M are built in the orthogonal direction and, thus, in the worst-case orientation. Since the structure built in the helix direction contains no flat overhang angles, the critical downskin areas are smooth even with cw exposure. Thus, it is assumed that the structure built in the helix direction gives the best possible flow results with low pressure drop p_{drop} at high flow velocities v_{flow} .

The absolute value of the pressure drop increases with the flow velocity. At constant flow velocities, the absolute pressure drop increases with the applied volume energy density using pulsed exposure. With decreasing volume energy density, the flow behavior improves. This is assumed to be caused by the tendentially lower downskin surface roughness proven in preliminary investigations [9]. Nevertheless, the density analyses disclosed a low density combined with an infiltration of the specimens for low energy densities. It should be mentioned that the flow behavior of the built structures is improved compared to the cw reference (black, dotted line). However, only very low energy densities lead to a flow curve similar to that of the best-case reference specimen (black, dash-dotted line). Two scenarios are possible:

1. The walls of the heat exchanger structures are permeable for a fluid flow. With this flow, the absolute value of the pressure drop could theoretically be lower than that of the best-case specimen (flatter curve in Fig. 11). Since only one of the flow curves exceeds that of the best-case specimen, other defects, such as high downskin rough-

ness at shallow overhang angles, surpass the positive impact of permeability.

2. There is no or a negligible flow through the walls with open porosity. In this case, the applied partial vacuum would not be high enough to allow the fluid to permeate the walls, or the permeation of the walls is too small to be noticed in the measurements. The dependency of the flow curves on the volume energy density can be explained by the roughness increase for higher volume energy densities demonstrated in [9]. The higher roughness causes increased friction in the fluid due to higher turbulences, resulting in an increased pressure drop.

The first scenario would not be detrimental to heat exchanger applications where mass transfer is acceptable, such as air-to-air heat exchangers. However, in principle, heat exchangers should contain impermeable walls. For this purpose, a parameter set above the threshold of open porosity would have to be used. To summarize the impact on the flow behavior, all specimens have a lower pressure drop than the specimens built with cw exposure in the same build direction. Specimens with densities above 97% show a significant improvement of the flow behavior towards the best-case variant (see solid black line in Fig. 11).

4 Conclusion

In this study, the influence of pulsed exposure strategies for support-free manufacturing of filigree overhang structures using laser-based powder bed fusion of metals is investigated. The study aims to apply the positive impacts of pulsed exposure described in the literature to specific technical components. A parametric study is conducted using a modified EOS M280 with Ti6Al4V as feedstock material. Solid cuboids and novel filigree heat exchanger structures are manufactured. The cuboids are used to analyze the density of resulting specimens. Dimensional accuracy and flow behavior are investigated on the heat exchanger structures.

The application of pulsed exposure strategies enables the support-free manufacturing of filigree structures with partial horizontal overhangs. Structures of this kind cannot be manufactured with sufficient quality using cw strategies. The results can be summarized as follows:

- Specimens with densities above 99% can be manufactured with pulsed exposure.
- Below a volume energy density of 30 J/mm^3 , the determined density values differ depending on the methodology used (optical and Archimedean method). This divergence in density values is caused by the penetration of the liquid during the Archimedean method. Conse-

quently, walls built with E_v below 30 J/mm^3 would be permeable.

- The geometric accuracy is independent of the process parameters in the range investigated. This is beneficial for the process robustness since there is no need to adjust parameters for various part areas like with cw exposure. The melt width is estimated to be $80 \mu\text{m}$.
- In the worst-case build orientation, the flow behavior could be significantly improved by using pulsed instead of continuous exposure. The pressure drop depends on the volume energy density applied. Specimens manufactured with lower volume energy density E_v result in lower absolute pressure drops. This behavior is attributed to a lower roughness.

For future investigations, it would be important to transfer the findings to other geometries and materials. Furthermore, the influence of the process parameters on the heat transfer between two channels should be investigated. Besides the pressure drop, this is the most important parameter of the heat exchanger. For these investigations, larger test specimens with corresponding fittings are necessary. The results shown are the foundation for these further studies.

Funding Open Access funding enabled and organized by Projekt DEAL.

Data availability The datasets generated during the current study are available from the corresponding author on reasonable request.

Declarations

Conflict of interest The authors declare that they have no competing interests.

Open Access This article is licensed under a Creative Commons Attribution 4.0 International License, which permits use, sharing, adaptation, distribution and reproduction in any medium or format, as long as you give appropriate credit to the original author(s) and the source, provide a link to the Creative Commons licence, and indicate if changes were made. The images or other third party material in this article are included in the article's Creative Commons licence, unless indicated otherwise in a credit line to the material. If material is not included in the article's Creative Commons licence and your intended use is not permitted by statutory regulation or exceeds the permitted use, you will need to obtain permission directly from the copyright holder. To view a copy of this licence, visit <http://creativecommons.org/licenses/by/4.0/>.

References

- Mertens R, Clijsters S, Kempen K, Kruth J-P (2014) Optimization of scan strategies in selective laser melting of aluminum parts with downfacing areas. *J Manuf Sci Eng*. <https://doi.org/10.1115/1.4028620>
- Hooper PA (2018) Melt pool temperature and cooling rates in laser powder bed fusion. *Addit Manuf* 22:548–559
- Han Q, Gu H, Soe S, Setchi R, Lacan F, Hill J (2018) Manufacturability of AlSi10Mg overhang structures fabricated by laser powder bed fusion. *Mater Des* 160:1080–1095
- Calignano F (2014) Design optimization of supports for overhanging structures in aluminum and titanium alloys by selective laser melting. *Mater Des* 64:203–213
- Jhabvala J, Boillat E, André C, Glardon R (2012) An innovative method to build support structures with a pulsed laser in the selective laser melting process. *Int J Adv Manuf Technol* 59(1–4):137–142
- Cooper K, Steele P, Cheng B, Chou K (2018) Contact-free support structures for part overhangs in powder-bed metal additive manufacturing. *Inventions* 3(1):2
- Mumtaz K, Hopkinson N (2009) Top surface and side roughness of Inconel 625 parts processed using selective laser melting. *Rapid Prototyp J* 15(2):96–103
- Mumtaz K, Hopkinson N (2010) Selective laser melting of Inconel 625 using pulse shaping. *Rapid Prototyp J* 16(4):248–257
- Grünwald J, Clarkson P, Salveson R, Fey G, Wudy K (2021) Influence of pulsed exposure strategies on overhang structures in powder bed fusion of Ti6Al4V using laser beam. *Metals* 11(7):1125
- Laag T, Winkel TM, Jauer L, Heußen D, Haefner CL (2022) Improvement of part accuracy by combination of pulsed wave (PW) and continuous wave (CW) laser powder bed fusion. *Berg Huettenmaenn Monatsh* 167(7):308–317
- Chou R, Milligan J, Paliwal M, Brochu M (2015) Additive manufacturing of Al-12Si alloy via pulsed selective laser melting. *JOM* 67(3):590–596
- Chen ZW, Guraya T, Singamneni S, Phan MAL (2020) Grain growth during keyhole mode pulsed laser powder bed fusion of IN738LC. *JOM* 72(3):1074–1084
- Biffi CA, Fiocchi J, Bassani P, Tuissi A (2018) Continuous wave vs pulsed wave laser emission in selective laser melting of AlSi10Mg parts with industrial optimized process parameters: Microstructure and mechanical behaviour. *Addit Manuf* 24:639–646
- Karami K, Blok A, Weber L, Ahmadi SM, Petrov R, Nikolic K, Borisov EV, Leeftang S, Ayas C, Zadpoor AA, Mehdipour M, Reinton E, Popovich VA (2020) Continuous and pulsed selective laser melting of Ti6Al4V lattice structures: effect of post-processing on microstructural anisotropy and fatigue behaviour. *Addit Manuf* 36:101433
- Caprio L, Demir AG, Previtali B (2018) Comparative study between CW and PW emissions in selective laser melting. *J Laser Appl* 30(3):32305
- Caprio L, Demir AG, Previtali B (2019) Influence of pulsed and continuous wave emission on melting efficiency in selective laser melting. *J Mater Process Technol* 266:429–441
- Demir AG, Previtali B (2017) Additive manufacturing of cardiovascular CoCr stents by selective laser melting. *Mater Des* 119:338–350
- Demir AG, Colombo P, Previtali B (2017) From pulsed to continuous wave emission in SLM with contemporary fiber laser sources: effect of temporal and spatial pulse overlap in part quality. *Int J Adv Manuf Technol* 91(5–8):2701–2714
- Demir AG, Mazzoleni L, Caprio L, Pacher M, Previtali B (2019) Complementary use of pulsed and continuous wave emission modes to stabilize melt pool geometry in laser powder bed fusion. *Opt Laser Technol* 113:15–26
- Laitinen V, Piili H, Nyamekye P, Ullakko K, Salminen A (2019) Effect of process parameters on the formation of single track in pulsed laser powder bed fusion. *Procedia Manufacturing* 36:176–183

21. Vasileska E, Demir AG, Colosimo BM, Previtali B (2020) Layer-wise control of selective laser melting by means of inline melt pool area measurements. *J Laser Appl* 32(2):22057
22. Vasileska E, Demir AG, Colosimo BM, Previtali B (2022) A novel paradigm for feedback control in LPBF: layer-wise correction for overhang structures. *Adv Manuf* 10(2):326–344
23. EOS GmbH - Electro Optical Systems (2016) *Bedienung - EOSINT M 280 / PSW 3.8*, Krailling / Munich.
24. Lee H, Lim CHJ, Low MJ, Tham N, Murukeshan VM, Kim Y-J (2017) Lasers in additive manufacturing: A review, *Int J Precis Eng Manuf Green Tech*, 4(3):307–22.
25. Tian Y, Tomus D, Huang A, Wu X Melt pool morphology and surface roughness relationship for direct metal laser solidification of Hastelloy X. *Rapid Prototyping Journal*.

Publisher's Note Springer Nature remains neutral with regard to jurisdictional claims in published maps and institutional affiliations.